

The response of relativistic outflowing gas to the inner accretion disk of a black hole

Michael L. Parker¹, Ciro Pinto¹, Andrew C. Fabian¹, Anne Lohfink¹, Douglas J. K. Buisson¹, William N. Alston¹, Erin Kara², Edward M. Cackett³, Chia-Ying Chiang³, Thomas Dauser⁴, Barbara De Marco⁵, Luigi C. Gallo⁶, Javier Garcia⁷, Fiona A. Harrison⁷, Ashley L. King⁸, Matthew J. Middleton⁹, Jon M. Miller¹⁰, Giovanni Miniutti¹¹, Christopher S. Reynolds², Phil Uttley¹², Ranjan Vasudevan¹, Dominic J. Walton¹, Daniel R. Wilkins⁸ & Abderahmen Zoghbi¹⁰

The brightness of an active galactic nucleus is set by the gas falling onto it from the galaxy, and the gas infall rate is regulated by the brightness of the active galactic nucleus; this feedback loop is the process by which supermassive black holes in the centres of galaxies may moderate the growth of their hosts¹. Gas outflows (in the form of disk winds) release huge quantities of energy into the interstellar medium², potentially clearing the surrounding gas. The most extreme (in terms of speed and energy) of these—the ultrafast outflows—are the subset of X-ray-detected outflows with velocities higher than 10,000 kilometres per second, believed to originate in relativistic (that is, near the speed of light) disk winds a few hundred gravitational radii from the black hole³. The absorption features produced by these outflows are variable⁴, but no clear link has been found between the behaviour of the X-ray continuum and the velocity or optical depth of the outflows, owing to the long timescales of quasar variability. Here we report the observation of multiple absorption lines from an extreme ultrafast gas flow in the X-ray spectrum of the active galactic nucleus IRAS 13224–3809, at 0.236 ± 0.006 times the speed of light (71,000 kilometres per second), where the absorption is strongly anti-correlated with the emission of X-rays from the inner regions of the accretion disk. If the gas flow is identified as a genuine outflow then it is in the fastest five per cent of such winds, and its variability is hundreds of times faster than in other variable winds, allowing us to observe in hours what would take months in a quasar. We find X-ray spectral signatures of the wind simultaneously in both low- and high-energy detectors, suggesting a single ionized outflow, linking the low- and high-energy absorption lines. That this disk wind is responding to the emission from the inner accretion disk demonstrates a connection between accretion processes occurring on very different scales: the X-ray emission from within a few gravitational radii of the black hole ionizing the disk wind hundreds of gravitational radii further away as the X-ray flux rises.

IRAS 13224–3809 is a low-redshift ($z = 0.0658$) NLS1 (Narrow Line Seyfert 1) galaxy. These galaxies are characterized by having low-mass, high-accretion-rate black holes⁵, some of which have evidence for relativistic outflows⁶. IRAS 13224–3809 is the most variable active galactic nucleus (AGN) in the X-ray band⁷, changing by up to two orders of magnitude in flux in only a few hours. This source was the target of a recent 1.5-Ms (about 17 days) continuous observing campaign with the X-ray Multi-Mirror Mission (XMM-Newton⁸) and 500 ks (almost 6 days) with the Nuclear Spectroscopic Telescope Array (NuSTAR) high-energy X-ray mission⁹ that was intended to study the

rapid variability of the AGN, from minutes to weeks. IRAS 13224–3809 is well known as a source with strong relativistic reflection from the inner disk¹⁰, where fluorescent emission, produced by X-ray illumination of the inner accretion disk, is blurred and skewed by the strong relativistic effects close to the event horizon. This produces a characteristic broad iron (Fe) line at 6–7 keV and a Compton scattered ‘hump’ at high energies. In this case, reflection spectroscopy revealed near-maximal spin, and a spectrum dominated by reflection, implying a high degree of light-bending close to the event horizon. The iron K and L lines can also be modelled as a relativistic absorption edge^{11,12}; however, the measurement of X-ray reverberation, which measures the delay between the continuum and reflected emission¹³, demonstrated that the line is produced by reflection and that we have an unobstructed view of the inner accretion disk.

The source is spectrally very soft, which is why the very-high-energy band (>8 keV) has not been well studied, owing to a shortage of photons in any given observation. By combining all the XMM-Newton EPIC-pn (the European photon imaging camera) data from the 2016 observing campaign into a single stacked spectrum and constraining the continuum flux using NuSTAR, we are able to reveal the presence of a structured absorption feature at about 8.6 keV in the rest frame of the source, significant at $>4\sigma$ (Fig. 1, top), along with a possible secondary line at about 9.2 keV. The 8.6-keV line is also present, at $>3\sigma$, in the stacked spectrum of the archival data (Extended Data Fig. 4), meaning that it must have been present for at least five years. Including the absorption line does not affect the results of reflection fitting; the parameters returned are entirely consistent with those found by previous authors^{10,14} (near-maximal spin, inclination of about 60°, and a steep emissivity profile).

Additional evidence for the presence of a ultrafast outflow is given by the simultaneous detection of three more blueshifted absorption lines in the high spectral resolution Reflection Grating Spectrometer (RGS¹⁵) data, which is capable of resolving narrow features at low energies. These features have a combined significance of $>5\sigma$, and are found at the same blueshift as the 8.6-keV line. Three broad features are detected at approximately 9.5 Å, 13.0 Å and 16 Å in the low-flux spectrum. They have less significance or are undetected in the higher-flux spectra with possible evidence of slight velocity change. Their wavelengths match with the strongest lines predicted by the photoionized ultrafast outflow model in the RGS energy band: 10.0 ± 0.5 Å (Ne x + Fe xviii–Fe xxii blend), 13.2 ± 0.5 Å (O viii K β + Fe xviii) and 15.8 ± 0.5 Å (O viii K α).

Depending on the ionization of the source, the 8.6-keV feature could be due to either Fe xxv or Fe xxvi, with corresponding outflow

¹Institute of Astronomy, Madingley Road, Cambridge CB3 0HA, UK. ²Department of Astronomy, University of Maryland, College Park, Maryland 20742-2421, USA. ³Department of Physics and Astronomy, Wayne State University, Detroit, Michigan 48201, USA. ⁴Remeis Observatory and ECAP, Universität Erlangen-Nürnberg, Sternwartstrasse 7, 96049 Bamberg, Germany. ⁵Max-Planck-Institut für extraterrestrische Physik, Giessenbachstrasse, 85748 Garching, Germany. ⁶Department of Astronomy and Physics, Saint Mary's University, 923 Robie Street, Halifax, Nova Scotia B3H 3C3, Canada. ⁷Space Radiation Laboratory, California Institute of Technology, 1200 East California Boulevard, MC 249-17, Pasadena, California 91125, USA. ⁸Kavli Institute for Particle Astrophysics and Cosmology, Stanford University, 452 Lomita Mall, Stanford, California 94305, USA. ⁹School of Physics and Astronomy, University of Southampton, Southampton SO17 1BJ, UK. ¹⁰Department of Astronomy, University of Michigan, 1085 South University Avenue, Ann Arbor, Michigan 48109, USA. ¹¹Centro de Astrobiología (CSIC-INTA), Departamento de Astrofísica, ESAC, PO Box 78, 28691 Villanueva de la Cañada, Madrid, Spain. ¹²Astronomical Institute Anton Pannekoek, University of Amsterdam, Postbus 94249, 1090 GE Amsterdam, The Netherlands.

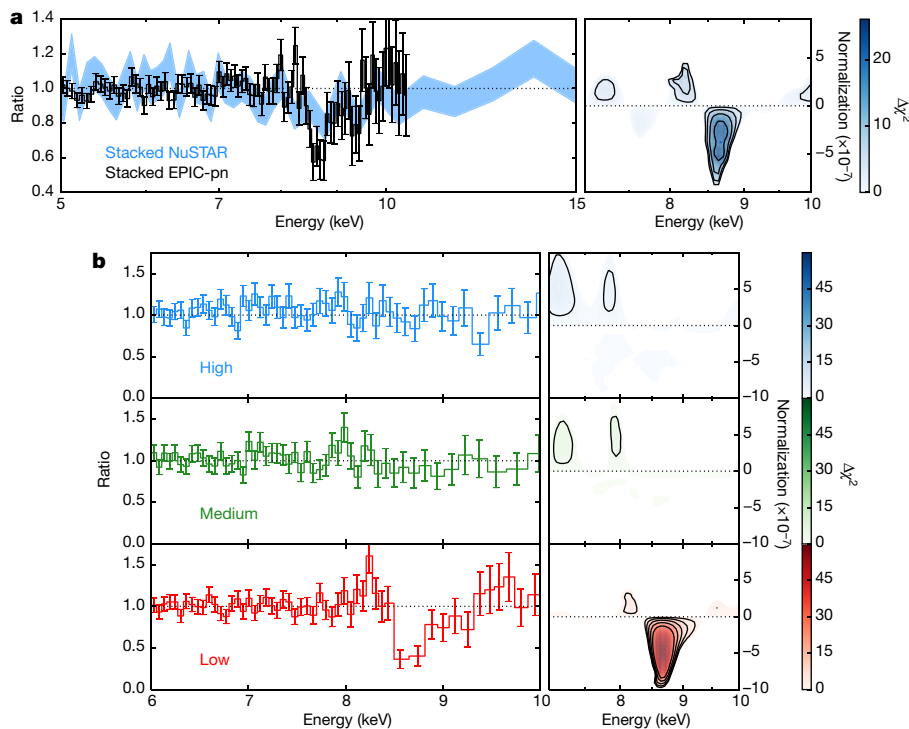


Figure 1 | High-energy absorption line detections. **a**, XMM-Newton EPIC-pn and NuSTAR residuals when fitted with a relativistic reflection model. A strong absorption feature is visible at about 8.6 keV. The right panel shows the results of a line search over this region, where the significance peaks at $>4\sigma$. **b**, Data-to-model ratio of stacked spectra of

IRAS 13224–3809 at three flux levels, fitted with a relativistic reflection model, and line search results. There is no significant absorption in the medium- or high-flux spectra, while in the low-flux state the line significance is about 7σ ($\Delta\chi^2 = 59.7$). Energies are in the source frame. Error bars are 1σ .

velocities of $0.24c$ or $0.21c$, where c is the speed of light in vacuum. However, a joint fit to the EPIC-pn and RGS data with a single absorber gives a best-fit velocity of $0.236 \pm 0.006c$, and robustly prefers the faster Fe xxv solution. The typical outflow velocity of radio-quiet AGN is about $0.1c$ (ref. 4), so the line identification puts this outflow in the fastest 5% or so of sources^{16,17}. The power output is also substantial. Assuming a solid angle $\Omega = 2\pi$, the kinetic power of the wind is around 4% of the Eddington luminosity (see Methods), comparable to the 15% found in the quasar PDS 456 (ref. 3), which is 2–3 orders of magnitude higher in mass (about $10^9 M_\odot$, where M_\odot is the mass of

the Sun, compared to about $6 \times 10^6 M_\odot$ for IRAS 13224–3809). This indicates that the wind in IRAS 13224–3809 may be capable of driving feedback. Similarly, the mass outflow rate is 0.4 times the Eddington accretion rate, implying that a large fraction of the mass is lost in the wind and that the accretion rate outside the wind launching radius may be super-Eddington. This is very similar to the wind found in the ultraluminous X-ray source^{18,19} NGC 1313 X-1, which also responds to changes in the continuum²⁰, implying that super-Eddington relativistic winds may be a common phenomenon in high-accretion-rate black holes^{21–23}.

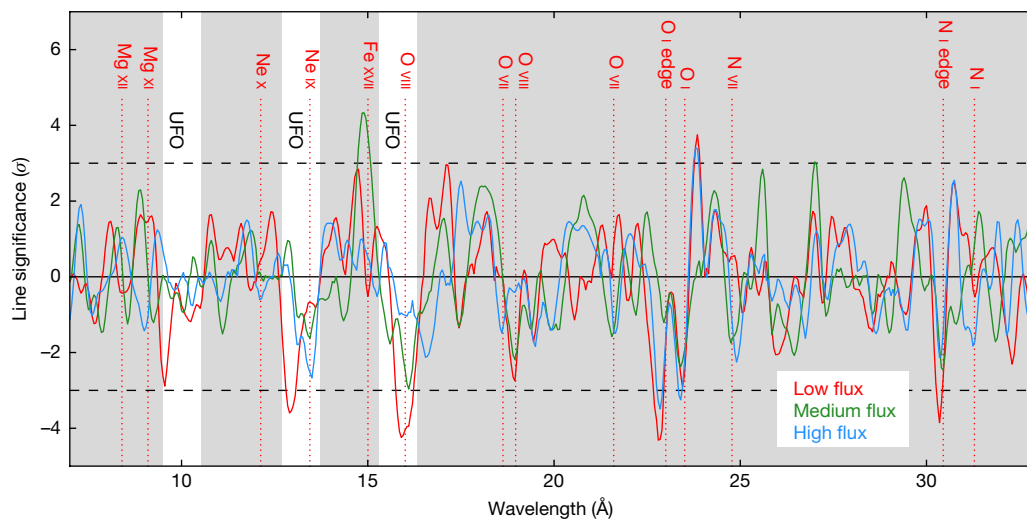


Figure 2 | RGS detection of flux-dependent absorption. Line significance obtained by a Gaussian fitting over the wavelength range 7–27 Å with increments of 0.05 \AA and negative values indicating absorption lines. The solid lines indicate the significance with widths of $1,000 \text{ km s}^{-1}$ for the three RGS spectra. The low-flux RGS spectrum is plotted in red, the

medium-flux spectrum in green, and the high-flux spectrum in blue. The rest-frame transitions of some relevant interstellar absorption lines are labelled. We highlight the regions (labelled UFO) where ultrafast-outflow absorption is predicted according to the spectral modelling of the EPIC data. Wavelengths are in the observed frame.

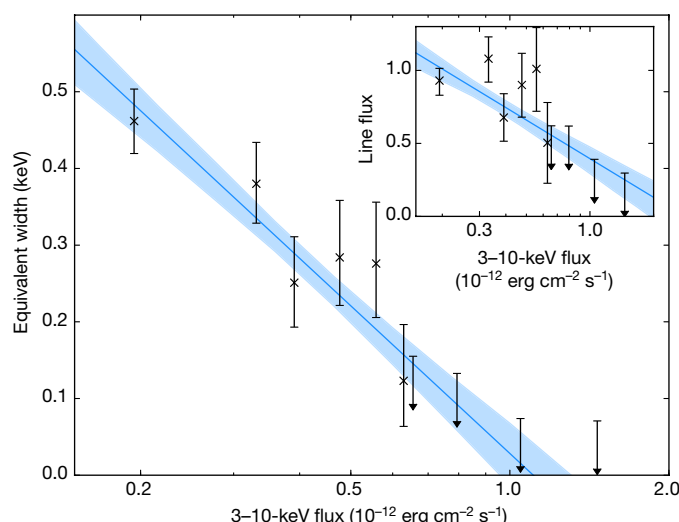


Figure 3 | Flux dependence of the outflow. Equivalent width of the EPIC-pn absorption line, plotted against the 3–10-keV flux, for ten flux-resolved spectra. A strong correlation is visible, and is fitted with a linear relation ($0.035 - 0.27 \log F$, blue line), calculated using Bayesian regression (which self-consistently takes into account the upper limits). Shaded regions show the 1σ confidence regions, calculated by drawing points from the posterior probability distribution. The inset shows the same correlation for the normalized (that is, multiplied by 10^6) line flux, which demonstrates that the change in equivalent width cannot be explained by a constant flux line. (Downward arrowheads indicate upper limits.) Error bars are 1σ .

IRAS 13224–3809 varies dramatically in flux on short timescales, giving us a unique opportunity to probe the fast variability of the wind. We split the large data set up into three different flux levels, such that the total number of counts in each of the three spectra is equal (Fig. 1). In the lowest-flux state, the line is extremely significant (7σ), with an equivalent width of 0.24 keV. However, when the flux is higher the line disappears completely, and is not statistically significant in the medium- and high-flux spectra. This variability of the 8.6-keV line strength must be occurring on relatively short timescales (<10 ks), because the source variability is so extreme that any delay in the absorption responding to the continuum flux would remove the observed correlation between the two. The average time between the end of a low-flux interval and the start of a high-flux interval is 4–5 ks, so the line must be responding within this time. Spectrally, the changes in the equivalent width can be explained by changes in either the column density or the ionization of the absorber. However, a causal relationship between the flux of the source and the ionization is expected, and both the flux and the model ionization increase by a factor of approximately four between the low- and high-flux spectra, consistent with the ionization interpretation. Because of the strong relativistic reflection observed in this source, we can be confident that we are seeing the inner regions of the AGN, and that the gas is responding directly to that emission.

The strength of the RGS absorption lines also anti-correlates with the flux, and therefore strongly argues in favour of the EPIC and RGS absorbers being part of the same extreme wind. In Fig. 2 we show the significance of the spectral features obtained adopting the (RGS fitted) spline continuum. We computed the confidence level of the three main absorption lines in the low-flux spectrum, where they are significantly detected, as with the EPIC-pn. We obtain 2.1σ , 2.9σ , and 3.4σ for the 9.5-Å, 13-Å, and 16-Å absorption lines, respectively, which, since they have the same velocity shift and broadening, gives a cumulative 5.1σ detection.

We investigate this in more detail by further subdividing the data into ten flux-resolved spectra, again with the same number of counts in each. Fitting these data with the same model and allowing the normalization of the Gaussian line to vary between them with the

velocity fixed gives a very strong correlation between the equivalent width of the line and the 3–10-keV flux (Fig. 3). The significance of this correlation is $>99.99\%$. This rapid variability clearly demonstrates that the outflow is responding to the source flux. Variability of outflows has been reported before⁴, but has never shown a clear correlation with the continuum behaviour.

However, the correlation we find could potentially be explained as the absorption lines disappearing owing to the increased ionization when the flux is high. Alternatively, this could be a geometric effect, where the line of sight from the X-ray corona intersects the wind at low source heights and misses it when the source is high or vertically extended, or the line could be produced in an ionized layer on the surface of the inner disk, absorbing the reflected emission only²⁴. Since the reflection fraction scales inversely with flux¹⁴, this could produce the observed correlation.

The discovery of a rapidly variable outflow, analogous to a quasar wind in velocity and outflow rate, in a low-mass, low-redshift AGN gives us insight into AGN feedback. The simultaneous detection of a relativistic outflow in the RGS and EPIC-pn spectra means that we can accurately characterize the physical properties of the wind, demonstrating that both sets of features can be produced by the same physical wind. The rapid variability, in a source where we can see clearly into the inner accretion disk, allows us to measure the disk wind at hundreds of gravitational radii responding to the X-rays originating a few gravitational radii away from the black hole, linking these physical processes—the inner disk accretion and the disk wind—occurring on these different scales. This work may allow us to uncover how relativistic winds are launched and accelerated.

Online Content Methods, along with any additional Extended Data display items and Source Data, are available in the online version of the paper; references unique to these sections appear only in the online paper.

Received 24 October 2016; accepted 9 January 2017.

- Silk, J. & Rees, M. J. Quasars and galaxy formation. *Astron. Astrophys.* **331**, L1–L4 (1998).
- Fabian, A. C. Observational evidence of active galactic nuclei feedback. *Annu. Rev. Astron. Astrophys.* **50**, 455–489 (2012).
- Nardini, E. et al. Galaxy evolution. Black hole feedback in the luminous quasar PDS 456. *Science* **347**, 860–863 (2015).
- Capri, M. et al. X-ray evidence for a mildly relativistic and variable outflow in the luminous Seyfert 1 galaxy Mrk 509. *Astron. Astrophys.* **504**, 401–407 (2009).
- Mathur, S. Narrow-line Seyfert 1 galaxies and the evolution of galaxies and active galaxies. *Mon. Not. R. Astron. Soc.* **314**, 17–20 (2000).
- Longinotti, A. L. et al. X-ray high-resolution spectroscopy reveals feedback in a Seyfert galaxy from an ultra-fast wind with complex ionization and velocity structure. *Astrophys. J.* **813**, L39 (2015).
- Ponti, G. et al. CAIXA: a catalogue of AGN in the XMM-Newton archive. *Astron. Astrophys.* **542**, A83 (2012).
- Jansen, F. et al. XMM-Newton observatory. I. The spacecraft and operations. *Astron. Astrophys.* **365**, L1–L6 (2001).
- Harrison, F. A. et al. The Nuclear Spectroscopic Telescope Array (NuSTAR) high-energy X-ray mission. *Astrophys. J.* **770**, 103 (2013).
- Fabian, A. C. et al. Long XMM observation of the narrow-line Seyfert 1 galaxy IRAS 13224–3809: rapid variability, high spin and a soft lag. *Mon. Not. R. Astron. Soc.* **429**, 2917–2923 (2013).
- Leighly, K. M., Mushotzky, R. F., Nandra, K., & Forster, K. Evidence for relativistic outflows in narrow-line Seyfert 1 galaxies. *Astrophys. J.* **489**, L25–L28 (1997).
- Boller, T. et al. XMM-Newton spectral properties of the narrow-line Seyfert 1 galaxy IRAS 13224–3809. *Mon. Not. R. Astron. Soc.* **343**, L89–L93 (2003).
- Kara, E., Fabian, A. C., Cackett, E. M., Miniutti, G. & Uttley, P. Revealing the X-ray source in IRAS 13224–3809 through flux-dependent reverberation lags. *Mon. Not. R. Astron. Soc.* **430**, 1408–1413 (2013).
- Chiang, C.-Y., Walton, D. J., Fabian, A. C., Wilkins, D. R. & Gallo, L. C. Modelling the extreme X-ray spectrum of IRAS 13224–3809. *Mon. Not. R. Astron. Soc.* **446**, 759–769 (2014).
- den Herder, J. W. et al. The Reflection Grating Spectrometer on board XMM-Newton. *Astron. Astrophys.* **365**, L7–L17 (2001).
- Tombesi, F. et al. Evidence for ultra-fast outflows in radio-quiet AGNs. I. Detection and statistical incidence of Fe K-shell absorption lines. *Astron. Astrophys.* **521**, A57 (2010).
- Gofford, J. et al. The Suzaku view of highly ionized outflows in AGN - I. Statistical detection and global absorber properties. *Mon. Not. R. Astron. Soc.* **430**, 60–80 (2013).

18. Pinto, C., Middleton, M. J. & Fabian, A. C. Resolved atomic lines reveal outflows in two ultraluminous X-ray sources. *Nature* **533**, 64–67 (2016).
19. Walton, D. J. *et al.* An iron K component to the ultrafast outflow in NGC 1313 X-1. *Astrophys. J.* **826**, L26 (2016).
20. Middleton, M. J. *et al.* Diagnosing the accretion flow in ultraluminous X-ray sources using soft X-ray atomic feature. *Mon. Not. R. Astron. Soc.* **454**, 3134–3142 (2015).
21. Shakura, N. I. & Sunyaev, R. A. Black holes in binary systems. Observational appearance. *Astron. Astrophys.* **24**, 337–355 (1973).
22. King, A. R. & Pounds, K. A. Black hole winds. *Mon. Not. R. Astron. Soc.* **345**, 657–659 (2003).
23. Poutanen, J., Lipunova, G., Fabrika, S., Butkevich, A. G. & Abolmasov, P. Supercritically accreting stellar mass black holes as ultraluminous X-ray sources. *Mon. Not. R. Astron. Soc.* **377**, 1187–1194 (2007).
24. Gallo, L. C. & Fabian, A. C. How the effects of resonant absorption on black hole reflection spectra can mimic high-velocity outflows. *Mon. Not. R. Astron. Soc.* **418**, L59–L63 (2011).

Acknowledgements M.L.P., C.P., A.C.F. and A.L. acknowledge support from the European Research Council through Advanced Grant on Feedback 340492. W.N.A. and G.M. acknowledge support from the European Union Seventh Framework Programme (FP7/2013–2017) under grant agreement number 312789, StrongGravity. D.J.K.B. acknowledges support from the Science and Technology Facilities Council. This work is based on observations with

XMM-Newton, an ESA science mission with instruments and contributions directly funded by ESA Member States and NASA. D.R.W. is supported by NASA through Einstein Postdoctoral Fellowship grant number PF6-170160, awarded by the Chandra X-ray Center, operated by the Smithsonian Astrophysical Observatory for NASA under contract NAS8-03060. This work made use of data from the NuSTAR mission, a project led by the California Institute of Technology, managed by the Jet Propulsion Laboratory, and funded by NASA. This research has made use of the NuSTAR Data Analysis Software (NuSTARDAS) jointly developed by the ASI Science Data Center and the California Institute of Technology.

Author Contributions M.L.P. wrote the manuscript with comments from all authors and performed the flux-resolved EPIC-pn analysis and line detections. C.P. analysed the RGS data and did the physical modelling. A.C.F. led the XMM-Newton proposal. All authors were involved with the proposal at various stages.

Author Information Reprints and permissions information is available at www.nature.com/reprints. The authors declare no competing financial interests. Readers are welcome to comment on the online version of the paper. Correspondence and requests for materials should be addressed to M.L.P. (mlparker@ast.cam.ac.uk).

Reviewer Information *Nature* thanks G. Risaliti and the other anonymous reviewer(s) for their contribution to the peer review of this work.

METHODS

Data reduction. We used all the available XMM-Newton data, both from our recent observing campaign (Principal Investigator A.C.F.) and from the archive. The EPIC-pn data are reduced using XMM-Newton's Science Analysis System (SAS) version 15.0.0 EPPROC (<https://www.cosmos.esa.int/web/xmm-newton/download-and-install-sas>) tool. The EPIC observations were made in large-window mode. We extracted source counts from a 30''-diameter circular region centred on the source coordinates, and background counts from a circular region about 60'' in diameter nearby on the same chip, avoiding contaminating sources, chip edges, and the region where the internal background due to copper is high, and filter the data for background flares. We created separate stacked spectra of the archival and new data using the ADDSPEC ftool (available as part of NASA's high-energy astrophysics software, HEASOFT; <http://heasarc.nasa.gov/lheasoft/>). We extracted full band (0.3–10 keV) lightcurves for each spectrum, shown in Extended Data Fig. 1, and divided the lightcurve into low-, medium- and high-flux intervals such that each flux band contained the same total number of counts (thus the low-flux intervals are much longer than the high-flux intervals). We then extracted spectra corresponding to each flux level from each observation, and combined them using ADDSPEC. We binned all the EPIC-pn spectra to achieve a signal-to-noise ratio of 6, after background subtraction, and to oversample the spectral resolution by a factor of 3.

The RGS camera consists of two similar detectors, which have high effective area and high spectral resolution between 7 Å and 38 Å. The second-order spectra cover the wavelength range 7–18 Å and provide double the spectral resolution. We corrected for contamination from soft-proton flares following the XMM-SAS standard procedures. For each exposure, we extracted the first- and second-order RGS spectra in a cross-dispersion region of 1' width, centred on IRAS sky coordinates. We extracted background spectra by selecting photons beyond 98% of the source point spread function. The background spectra were consistent with those from blank field observations. Using the SAS task RGSCOMBINE, we stacked all RGS 1 and 2 spectra, obtaining two high-quality spectra for both the first and the second order with a total, clean exposure of 1.529 Ms each. We grouped the RGS spectra in channels equal to one-third of the point spread function, and use C-statistics, because it provides optimal spectral binning and avoids over-sampling. RGS spectral fitting is performed using the SPEX package (<https://www.sron.nl/astrophysics-spx>), with contributions from XSPEC, in particular for reflection models. Flux-resolved spectra are extracted using the same good-time-interval files as used for the EPIC-pn analysis.

The NuSTAR data were reduced using the NuSTAR data analysis software (NuSTARDAS) version 1.6.0 and CALDB version 20160731. We extracted source counts from a 30''-diameter circular region, centred on the source, and background counts from a large circular region on the same chip. We combined all the NuSTAR data into a single spectrum, given that the count rate is very low due to the extremely soft spectrum, and binned to achieve a signal-to-noise ratio of 6 and oversampling of 3.

Pile-up. In the high-flux intervals, the source flux is above the nominal EPIC-pn large-window-mode pile-up limit of 3 counts s⁻¹ (ref. 23), reaching about 9 counts s⁻¹ at times. This risks distorting the spectrum and potentially affecting the detection of the ultrafast outflow. However, the count rate of IRAS 13224–3809 is dominated by photons from below 1 keV (the count rate from 0.5 keV to 1 keV is an order of magnitude higher than the count rate from 2 keV to 3 keV), because it is an extremely soft source. This means that the effects of pile-up are strongest below 2–3 keV. We tested this by extracting the same high-flux spectrum using an annular region, instead of a circle, with an excised core of 7'', which encircles the central four piled-up pixels. Above 2 keV, we found no difference in spectral shape between the two spectra, so we conclude that our analysis (restricted to $E > 3$ keV) is robust to this effect. The absorption feature is still present in both the mean spectrum and the low-flux spectrum when an annular extraction region is used. We also repeated this test using only single events, and again found no difference. The low-flux spectrum and the RGS spectra are not affected by pile-up.

Copper contamination. One potential cause of a false detection of an ultrafast outflow around 8 keV is the complex of emission lines, dominated by Cu K α , in the instrumental background²⁶. Over-subtracting these features would result in an artificial absorption feature at the corresponding energy, which would depend on the source to background flux ratio, giving an anticorrelation between the equivalent width of the line and the source flux. The copper background is only high in the outer regions of the detector, outside the central 300'', leaving a central 'hole' where contamination is minimal. We were careful to avoid the region where the copper background is high when selecting background regions, which should prevent contamination (see Extended Data Fig. 2). The easiest way to show that the ultrafast-outflow line is not an artefact of background over-subtraction is simply to not subtract the background and check the line remains. Although this is not always optimal (it may remove genuine but weak lines, or introduce new features),

strong absorption features should remain in the spectrum. In Extended Data Fig. 3, we show the low-flux spectrum with no background subtraction, fitted with a power law. The iron line is weaker, owing to the additional high-energy contribution from the background, but the ultrafast-outflow line is clearly still present. If the observed line were produced by over-subtraction of the background, the (negative) flux of the line should be constant, the equivalent of an additional constant (positive) line in the background. This is trivial to test, by measuring the strength of an additive line with flux, rather than the multiplicative line we use elsewhere. We find clear variability, and an anti-correlation between the line flux and source flux (Fig. 3, inset), which is impossible if the line is a background feature. Finally, we note that the lines seen in the RGS spectrum are independent of this effect. We conclude that the line is genuine, and produced by absorption in the AGN spectrum.

The potential secondary feature at about 8.7 keV (observer's frame, 9.2-keV source frame) is coincidental with the Zn K α line, and appears as an emission feature when the background is not subtracted. We cannot therefore robustly determine whether it is a genuine spectral feature, a statistical fluctuation, or due to the background.

EPIC-pn/NuSTAR stacked spectra. We fitted the stacked 2016 EPIC-pn spectrum in the range 3–10 keV (outside the band where pileup effects are present, and where the spectrum is relatively simple and unambiguous), and the stacked NuSTAR spectrum in the range 3–40 keV. We modelled the spectrum with the RELXILL relativistic reflection model²⁷. The relativistic blurring parameters are consistent with those found by previous authors¹⁰ (see Extended Data Table 1), but a strong absorption feature remains at around 8.6 keV. When we included an additional Gaussian absorption line (modelled with GABS, with σ_{Gauss} fixed at 0.1 keV), the fit improved by $\Delta\chi^2 = 26$, for two additional free parameters (degrees of freedom). Parameters for both these models are given in Extended Data Table 1. We also tested allowing σ_{Gauss} to vary, but we found no significant difference in the fit statistic and no impact on the other fitting parameters.

There are some differences between this result and those found by previous authors, which probably stem from the different energy range used. In particular, the photon index, the high-energy cut-off, and the iron abundance are different. The continuum parameters are not of great importance to this work, so long as the continuum is adequately described. The steeper Γ value in archival results (about 2.7; ref. 14) is probably due to the inclusion of the soft excess, which past authors^{10,14} have fitted with a two-component reflection model. This requires a steep power law to produce enough soft photons to fit the soft excess. This model is not unique, because the soft excess generally has limited spectral features owing to the lower resolution of the EPIC-pn at these energies, and other factors, such as density of the disk, may alter the parameters from such a fit²⁸. A visual comparison of the archival data and the new data (Extended Data Fig. 4a) does not show any major changes in the structure of the iron line or ultrafast-outflow absorption.

Similarly, the iron abundance is largely determined by the relative strengths of the iron line and soft excess or Compton hump. Given the steep power law in the dual-reflection model, a high iron abundance is required to produce enough flux in the iron line. This is not required here, as we did not fit the soft excess and the Compton hump is only weakly constrained. This is important, as the iron abundance is potentially degenerate with the strength of the 8.6-keV absorption feature: an increased iron abundance produces a larger iron absorption edge in the reflection spectrum. We can be confident that this is not having a significant effect on our results, because the iron abundance is free to vary in all our fits, including the fits without the absorption modelled, and the feature still remains. We have explicitly searched for degeneracies using a Markov Chain Monte Carlo, and find no degeneracy between the strength of the line and the iron abundance.

Following on from this, we performed a blind line scan over the 6–10-keV band, stepping an unresolved Gaussian line ($\sigma_{\text{Gauss}} = 0.01$, allowed to be positive or negative) across the energy band, varying the normalization, and recording the $\Delta\chi^2$ at each point on this grid (Fig. 1a). We use the same underlying RELXILL model, allowing the same parameters to vary. We calculate the significance of this by taking the probability of the maximum $\Delta\chi^2$ for two additional free parameters, and correcting by the number of trials (that is, the number of resolution elements from 6.7 keV to 10 keV). This gives a final chance probability of 1.5×10^{-5} , which corresponds to a 4.3 σ detection. No other features are significant above about 1 σ .

We also fitted the absorption with a series of physical models—WARMABS in XSPEC (shown in Extended Data Fig. 4b), which uses grids of XSTAR photoionization models, and XABS and PION in SPEX. The three models give consistent results, with a degeneracy between two possible solutions with outflow velocities of $v = 0.210 \pm 0.009$ and $v = 0.244 \pm 0.09$, corresponding to Fe xxv and Fe xxvi. These solutions have different column densities and ionizations, which are summarized in Extended Data Table 2. The velocity broadening is not strongly constrained, but does not appear to affect any of the other wind parameters.

We test this by fixing the broadening to lower and higher values, and find no change in the column density, velocity or ionization of the fit.

RGS stacked spectrum. The RGS spectrum is complex, showing several broad emission-like features at 15 Å and 18 Å. This spectrometer is the most sensitive to narrow ($\lesssim 1,000$ Å) features, but higher effective area and broader energy range EPIC detectors are more efficient for determining the spectral continuum. We therefore performed an independent analysis of the RGS spectra using either a phenomenological spline continuum model fitted to the RGS spectrum or the physical reflection model provided by the best-fit reflection (RELXILL) model of the EPIC-pn stacked spectrum. When fitting the RGS spectrum, the spline is corrected for redshift and Galactic interstellar-medium absorption. We search for features in the RGS spectrum following an advanced procedure¹⁸. We include a Gaussian spanning the wavelength range 7–38 Å in increments of 0.05 Å, and assume a linewidth of 1,000 km s^{−1} (comparable to the RGS resolution). This broadening will also tend to strengthen the detection of any warm-absorber and ultrafast-outflow lines with respect to interstellar absorption lines, since the latter are typically narrower²⁹ (≤ 200 km s^{−1}). We take into account the absorption edges of neutral neon (14.3 Å), iron (17.5 Å), and oxygen (23.0 Å), but we exclude the corresponding 1s–2p absorption lines in order to detect and compare any spectral feature intrinsic to IRAS 13224–3809 or to the interstellar medium. The strongest non-Galactic absorption feature detected is a broad depression around 16 Å, which is also clear in the RGS stacked spectrum (see Extended Data Fig. 5). The other two putative, weaker, absorption-like features appear at 10 Å and 13 Å. Interestingly, the photoionization model of the EPIC spectrum predicts three broad (about 1,500 km s^{−1}) ultrafast-outflow absorption lines that match the three RGS absorption features. We have tested different linewidths (from 100 km s^{−1} to 5,000 km s^{−1}) without finding a major effect on their detection. The significance of the rest-frame absorption lines of Galactic O VII and O VIII instead increase up to 5 σ for narrower widths (< 200 km s^{−1}), confirming the results obtained with the grating spectra of the brightest X-ray binaries²⁹.

A full description of the RGS spectral modelling and the corresponding flux-resolved high-resolution X-ray spectroscopy will be discussed in a forthcoming paper. Here we provide the main result obtained with the overall spectrum and a first interpretation of the wind variability. We modelled the RGS stacked spectrum with both a spline and a reflection continuum in order to constrain the characteristics of the ultrafast outflow. The interstellar medium was modelled following the detailed multi-phase gas model constrained with the low-mass X-ray binaries²⁹. We modelled the ultrafast-outflow absorption features in the RGS spectrum with an outflowing gas in photoionization equilibrium (XABS model in SPEX 3.02). The best fit of the RGS stacked spectrum provides the column density $N_{\text{H}} = 9.5 \pm 0.5 \times 10^{22}$ cm^{−2} (90% error) the ionization parameter $\log \xi = 4.0 \pm 0.1$ erg cm s^{−1} and the linewidth $\sigma_v = 2,000 \pm 1,000$ km s^{−1}. The RGS velocity shift $v = -0.231c \pm 0.007c$ fits between the EPIC Fe xxv ($-0.244c \pm 0.009c$) and the Fe xxvi ($-0.210c \pm 0.009c$) solutions, and does not fully constrain which solution is most likely, but slightly prefers the Fe xxv ($-0.244c$) solution, which is consistent within the 90% confidence level.

Joint fit. We investigate a combined fit to both EPIC-pn and RGS spectra, fitting with the same absorption model but different continuum models for each spectrum (the physical reflection model for the EPIC-pn, and a spline for the RGS). We also include a photoionized emission component, modelled with the XSPEC PHOTEMIS model. The soft and hard absorption features are consistent with being from the same absorber (freeing the parameters between the two results in an improvement to the fit of only $\Delta\chi^2 = 3$, for four additional free parameters). The joint fit clearly prefers the Fe xxv solution, with final best-fit parameters of $v = 0.236c \pm 0.006c$, $\sigma_v = 4,000 \pm 1,000$, $\log \xi = 4.14 \pm 0.13$ and $N_{\text{H}} = 2.2_{-1.6}^{+0.8} \times 10^{23}$ cm^{−2}. The increased broadening with respect to the individual spectrum fits may be due to a small offset between the EPIC-pn and RGS spectra, which could be caused by gain shift in the EPIC-pn. However, it is consistent at the 90% level with that found from the RGS alone.

The inclusion of the emission component improves the fit significantly ($\Delta\chi^2 = 21$, for two additional free parameters), accounting for the residuals at about 8.3 keV and other possible features. The velocity of this component is $0.213c \pm 0.015c$, and the luminosity is $(1.1 \pm 0.5) \times 10^{41}$ erg s^{−1}. If this component is genuine, it is made up of scattered emission from the wind, and can in principle be used to determine the wind geometry. However, it is likely that much of the P Cygni profile, including any redshifted emission, is obscured by the relativistic iron line, which is very strong in this source. One possible approach to take here would be to search for the emission component of the P Cygni profile in the lag spectra, as the reverberation timescale should be much longer than for the relativistic reflection component, owing to the greater distance from the source.

EPIC-pn flux-resolved spectra. We also fitted the three flux-resolved spectra, tying parameters we expect to be constant (such as a and i) between the different spectra. The model parameters are consistent with those given in Extended Data

Table 1, with the reflection fraction inversely proportional to flux. We performed the same line scan over these spectra simultaneously, stepping the line across in energy then recording the $\Delta\chi^2$ for each spectrum individually. The line is only significantly detected in the low flux spectrum, with a maximum $\Delta\chi^2$ of 59.7, for two additional free parameters. This gives a corrected probability of 1.96×10^{-12} , and a significance of 7.0 σ .

We also check the robustness of the low-flux line detection using a Monte Carlo test. We draw parameters from a Markov chain Monte Carlo, used to evaluate the errors and degeneracies in the best-fit parameters, and use them to simulate 10,000 fake spectra. We then fitted these spectra using the same procedure. None of the simulated spectra have higher significance features, in either emission or absorption, setting a lower limit of $P > 99.99\%$ on the significance. Given the expected fraction of 4.6×10^{-12} , it is not feasible to test sufficient spectra to establish the true significance using this method.

We performed a similar analysis with ten flux-resolved spectra, again with the same number of counts in each. We fitted the spectra simultaneously, using RELXILL and a Gaussian absorption line, allowing the reflection fraction, power-law index, and normalizations of the reflection and Gaussian components to vary between each spectrum. This gives a reasonable fit ($\chi^2/\text{d.o.f.} = 966/857 = 1.13$, where d.o.f. is degrees of freedom). We then recorded the equivalent width and flux of the absorption line in each spectrum, and the 3–10-keV flux. These are plotted against each other in Fig. 3, showing a strong correlation. We used Bayesian regression to perform a linear fit, which incorporates the upper limits, and draw samples from the posterior distribution to calculate the uncertainty. We calculated the probability of a stronger correlation being found from a constant absorption feature by simulating 10,000 sets of points with the same errors, assuming that the line strength is constant in each case, and performing the same analysis. In no case did we find a stronger correlation.

RGS flux-resolved spectra. We performed high-resolution flux-resolved X-ray spectroscopy with the RGS data, consistent with that performed with EPIC: we extracted RGS 1 and 2 first- and second-order spectra with the good time intervals defined according to the EPIC flux prescriptions. We stacked the RGS 1 and 2 spectra for each flux range, obtaining three high-quality RGS spectra with comparable statistics. As previously seen for the overall stacked spectrum, there are some non-interstellar absorption-like features (at 9.5 Å, 13 Å and 16 Å) which show evidence of variability, being both stronger and possibly bluer in the low-flux spectrum. To probe the strength of the features in each spectrum, we applied the same technique used for the stacked spectrum by fitting a Gaussian over the wavelength range 7–38 Å in increments of 0.05 Å. In Fig. 2, we show the significance of the spectral features obtained adopting the (RGS fitted) spline continuum. The three broad features were still detected at 9.5 Å, 13.0 Å and 16 Å in the low-flux spectrum. They have less significance or are undetected in the higher-flux spectra with possible evidence of slight velocity change. Their wavelengths match with the strongest lines predicted by the 0.24c ultrafast outflow model in the RGS energy band: 10.0 ± 0.5 Å (Ne x + Fe xviii–Fe xxii blend), 13.2 ± 0.5 Å (O viii K β + Fe xviii) and 15.8 ± 0.5 Å (O viii K α). The strength of the absorption lines anti-correlate with the flux in agreement with the EPIC result and therefore provides strong evidence in favour of a connection between the EPIC and RGS absorbers as being part of the same extreme wind. We computed the confidence level of the three main absorption lines in the low-flux spectrum, where they are significantly detected as in EPIC. Accounting for the number of trials due to bins of 0.05 Å and an outflow-velocity range from 0c to 0.3c, we obtain 2.1 σ , 2.9 σ and 3.4 σ for the 9.5-Å, 13-Å and 16-Å absorption lines, respectively, which—since they have the same velocity shift—gives a cumulative 5.1 σ detection. **Energetics.** We can estimate the mass outflow rate by combining the velocity and column densities³, and the mass³⁰ of $6 \times 10^6 M_{\odot}$ (estimated using the empirical reverberation relation³¹):

$$\dot{M} = \Omega N_{\text{H}} m_{\text{p}} v R_{\text{wind}} \quad (1)$$

where Ω is the solid angle of the wind and R_{wind} is the radius of the wind.

We cannot be confident of the value of Ω , as the emission from the P Cygni profile, if there is any, is obscured by the blue horn of the iron line, which is extremely strong in this source. However, given that the absorption line is found in the stacked archival data (most of which is from 2011), this implies that the feature has been present and roughly constant (as a function of flux) for at least 5 years, which would argue for a reasonably large covering fraction, otherwise any clump along the line of sight would probably have moved away. Similarly, we do not know the radius of the wind. However, we know that it must be variable on timescales $\lesssim 5$ ks, which corresponds to 170 gravitational radii (R_g). Assuming a radius of $100 R_g$, we find the accretion rate $\dot{M} = 2 \times 10^{23} \times \Omega \text{ g s}^{-1}$ ($0.03 \Omega M_{\odot} \text{ year}^{-1}$) for Fe xxv, while the Eddington accretion rate for a black hole of this mass is $2.7 \times 10^{24} \text{ g s}^{-1}$, assuming an efficiency of 0.3 for near-maximal spin. In either case,

a large fraction of the matter accreted by the disk is lost to the wind, possibly implying super-Eddington accretion at large radii (beyond R_{wind}).

We can then calculate the power in the wind:

$$\begin{aligned} P &= \frac{1}{2} \dot{M} v^2 \\ P &= 0.006 \Omega L_{\text{Edd}} \end{aligned} \quad (2)$$

For $\Omega = 2\pi$, this gives a power of 4% of the Eddington luminosity L_{Edd} , implying that a non-negligible fraction of the accretion power must be lost into the wind. For the same assumed covering fraction, the power of the quasar PDS 456 is 15% of the Eddington luminosity³.

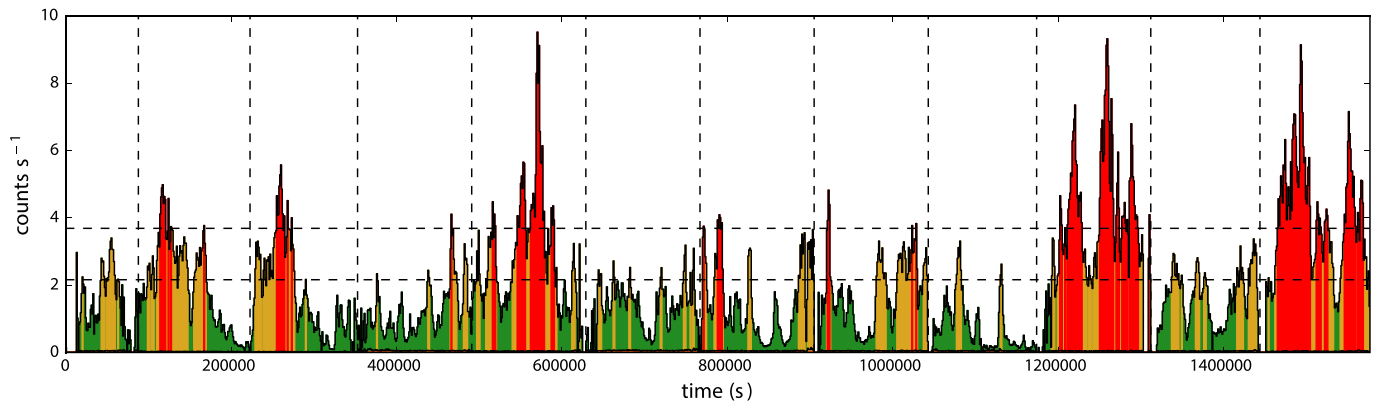
Alternative interpretations. The prevailing interpretation for highly blueshifted absorption features in the X-ray spectra of AGNs is that they are due to outflowing gas. However, it is possible that some of these features may instead be due to absorption by a diffuse absorbing surface layer on the approaching side of the accretion disk, which naturally gives relativistic velocities³². The absorption line then appears in the reflection component. Aberration means that the blue side is brighter than the red side. For a disk inclination of 60° the absorption layer needs to extend from about $5R_g$ to $10R_g$ to give an observed line at 8.2 keV. If the brighter parts of the light curve are associated with the corona rising above $10R_g$, then reduced light bending and irradiation of the inner disk weakens both the reflection component and the absorption, consistent with observation.

It is also possible that the variability is produced by a geometric effect. Previous authors have suggested that the relatively constant spectrum of the relativistic reflection component can be produced by changes in the height or extent of the X-ray corona above the disk³³, and the covering fraction of a wind at a small angle to the disk could similarly depend on the size or position of the compact X-ray source. **Code availability.** All the code used for the data reduction is available from the respective websites. XSPEC and SPEX are freely available online. Code used for

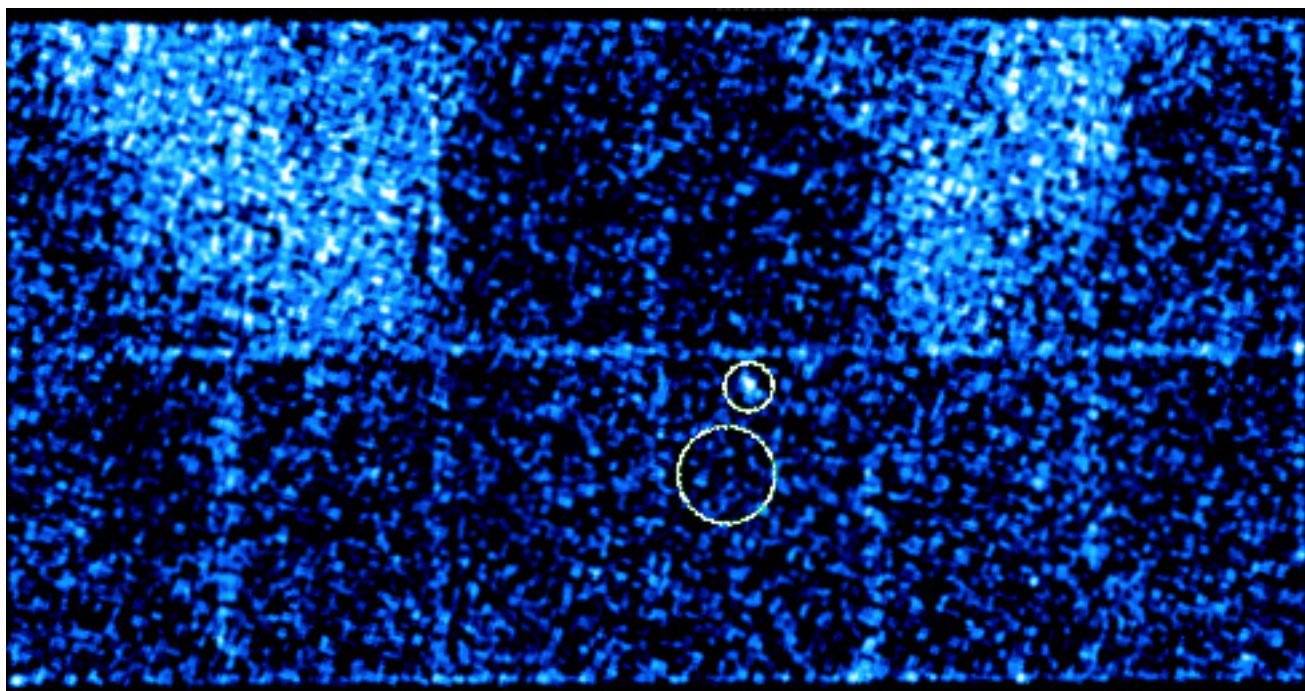
generating figures, calculating flux-resolved extraction intervals, and calculating line significance, is available upon request to M.L.P.

Data availability statement. All data used in this work is publicly available. The XMM-Newton observations can be accessed from the XMM-Newton science archive (<http://nxsas.esac.esa.int/nxsas-web/>) and the NuSTAR data from the HEASARC archive (<http://heasarc.gsfc.nasa.gov/docs/archive.html>). Figure data are available from the authors.

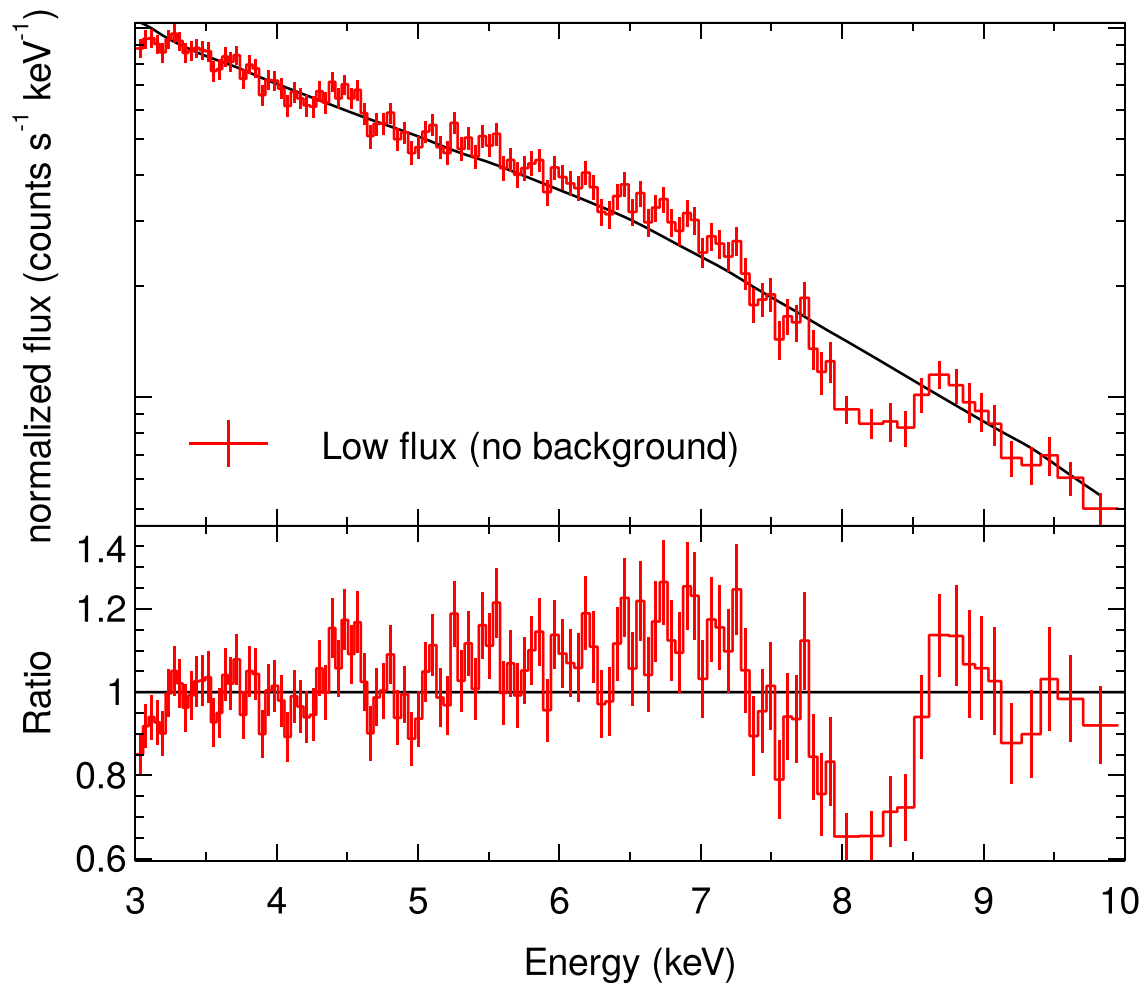
25. Jethwa, P., Saxton, R., Guainazzi, M., Rodriguez-Pascual, P. & Stuhlinger, M. When is pile-up important in the XMM-Newton EPIC cameras? *Astron. Astrophys.* **581**, A104 (2015).
26. Freyberg, M. J. *et al.* EPIC pn-CCD detector aboard XMM-Newton: status of the background calibration. *Proc. SPIE* **5165**, 112 (2004).
27. García, J. *et al.* Improved reflection models of black hole accretion disks: treating the angular distribution of X-rays. *Astrophys. J.* **782**, 76 (2014).
28. García, J. A. *et al.* The effects of high density on the X-ray spectrum reflected from accretion discs around black holes. *Mon. Not. R. Astron. Soc.* **462**, 751–760 (2016).
29. Pinto, C., Kaastra, J. S., Costantini, E. & de Vries, C. Interstellar medium composition through X-ray spectroscopy of low-mass X-ray binaries. *Astron. Astrophys.* **551**, A25 (2013).
30. Zhou, X.-L. & Wang, J.-M. Narrow iron $K\alpha$ lines in active galactic nuclei: evolving populations? *Astrophys. J.* **618**, L83–L86 (2005).
31. Kaspi, S. *et al.* Reverberation measurements for 17 quasars and the size-mass-luminosity relations in active galactic nuclei. *Astrophys. J.* **533**, 631–649 (2000).
32. Gallo, L. C. & Fabian, A. C. The origin of blueshifted absorption features in the X-ray spectrum of PG 1211+143: outflow or disc. *Mon. Not. R. Astron. Soc.* **434**, L66–L69 (2013).
33. Miniutti, G. & Fabian, A. C. A light bending model for the X-ray temporal and spectral properties of accreting black holes. *Mon. Not. R. Astron. Soc.* **349**, 1435–1448 (2004).



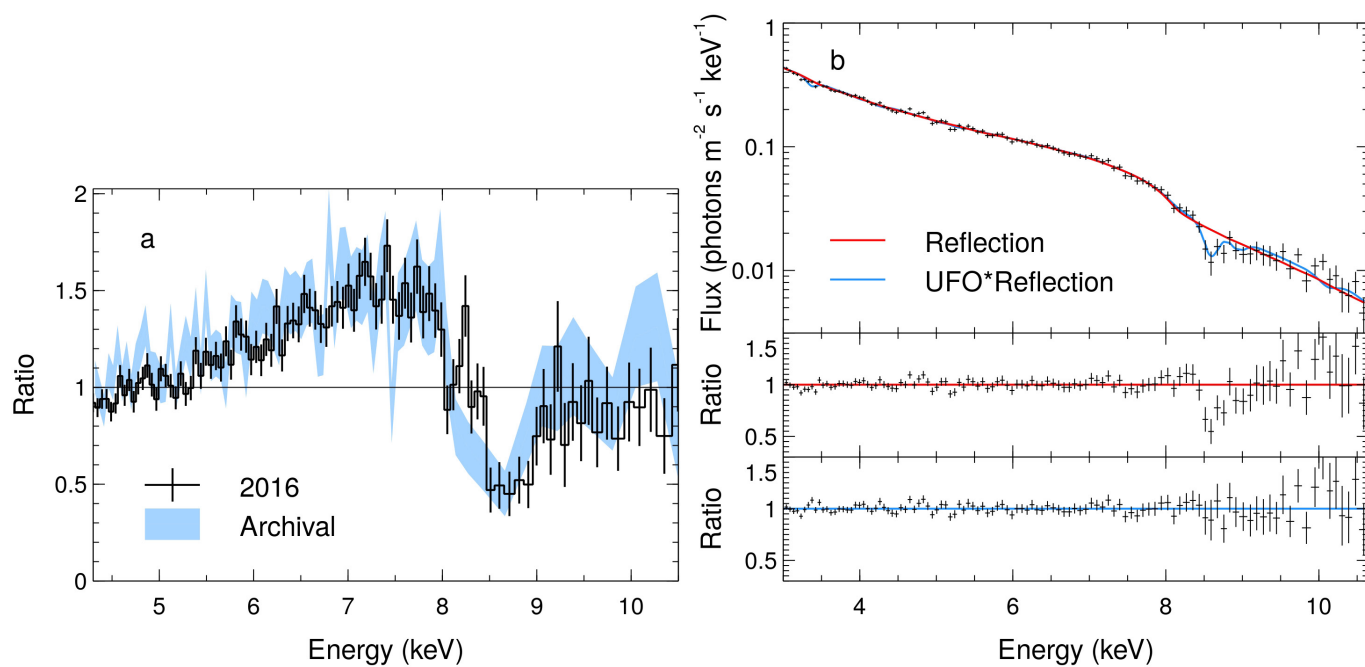
Extended Data Figure 1 | The 0.3–10-keV lightcurve of the new observations of IRAS 13224–3809. We use 1-ks bins, with gaps between observations removed. The vertical dashed lines show where observations start and finish, and the horizontal dashed lines show the threshold flux levels. Low-, medium- and high-flux intervals are distributed throughout the lightcurve, and are coloured green, yellow and red, respectively.



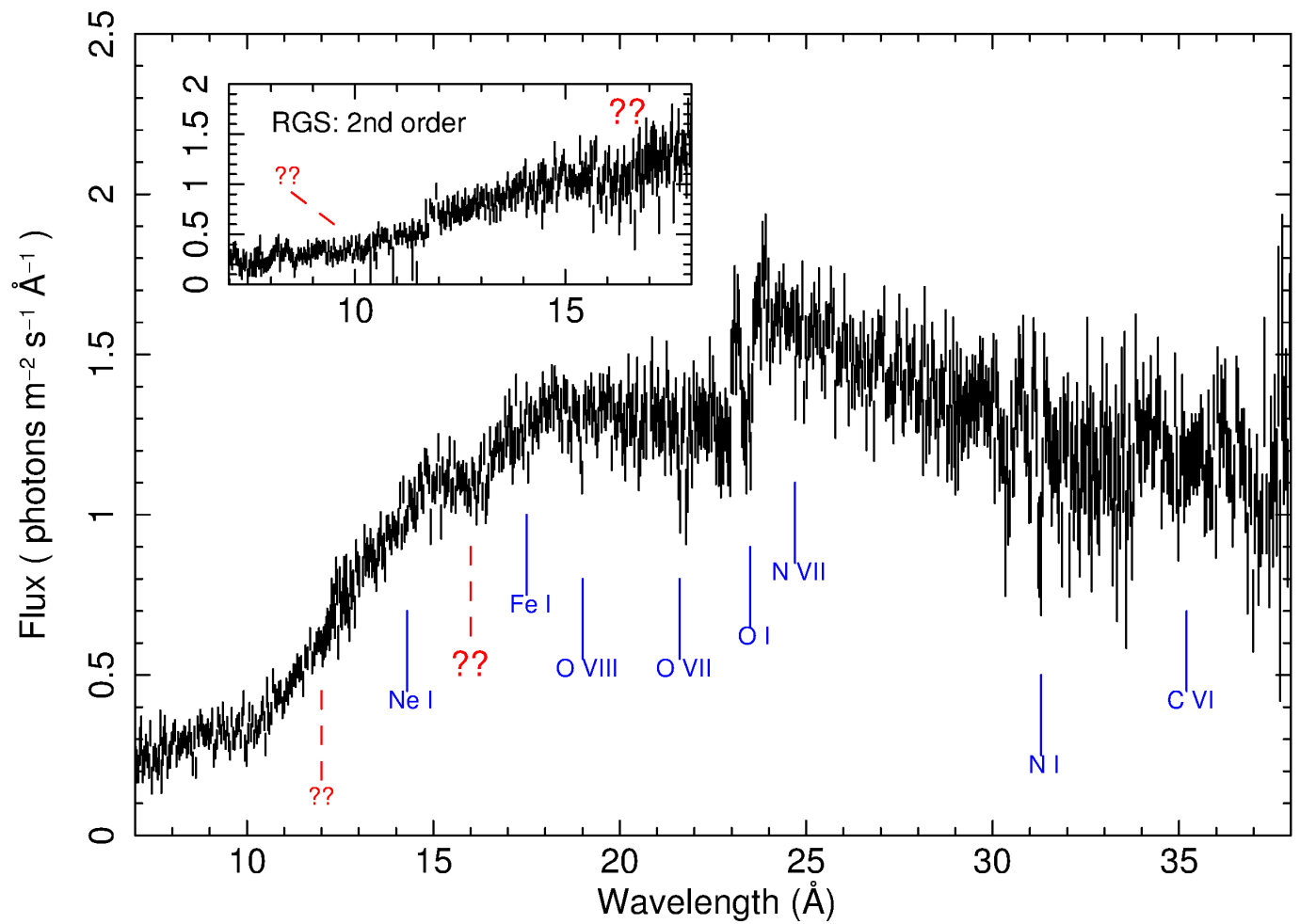
Extended Data Figure 2 | The 8–8.5-keV EPIC-pn image showing the high instrumental background outside the central chips. Source and background extraction regions marked by small and large white circles, respectively, for a representative observation (0780561301).



Extended Data Figure 3 | The low-flux spectrum without background subtraction. The spectrum is fitted with a power law. The ultrafast-outflow line is clearly still visible in the residuals, and only slightly reduced in strength. All errors are $\pm 1\sigma$, and energies are in the observer's frame. 'Ratio' indicates the ratio of data to model output.



Extended Data Figure 4 | EPIC-pn spectroscopy. **a**, Data and residuals of the EPIC-pn data fitted with reflection, with and without an outflowing absorption component. **b**, Residuals of the EPIC-pn data fitted with a power law from 4–5 keV and 9–10 keV, showing the broad iron line and ultrafast-outflow (UFO) line. Error bars are 1σ , and energies are in the source rest frame.



Extended Data Figure 5 | RGS first-order and second-order (small panel) stacked spectra of all 17 observations. Transitions of typical interstellar absorption lines are labelled. Additional features of non-interstellar-medium origin are indicated with a dashed red line and two question marks. Above 33 \AA the RGS spectrum is affected by high background. Error bars are 1σ , and energies are in the source rest frame.

Extended Data Table 1 | Phenomenological model fit

Parameter	Model 1	Model 2	Description/unit
E_{Gauss}	-	8.14 ± 0.03	Line energy (keV)
σ_{Gauss}	-	0.1*	Line width (keV)
N_{Gauss}	-	0.15 ± 0.03	Line strength
q_{in}	> 8.5	$8.3^{+0.2}_{-1.2}$	Inner emissivity index
q_{out}	2.4 ± 0.1	2.46 ± 0.04	Outer emissivity index
r_{break}	$2.52^{+0.1}_{-0.07}$	2.59 ± 0.04	Emissivity break radius (r_{G})
a	> 0.994	0.989 ± 0.001	Black hole spin
i	60 ± 0.1	59 ± 1	Inclination (degrees)
Γ	$1.99^{+0.12}_{-0.06}$	$2.06^{+0.06}_{-0.09}$	Power-law index
E_{cut}	50^{+17}_{-15}	50 ± 6	Power-law cutoff energy (keV)
$\log \xi$	$3.25^{+0.06}_{-0.09}$	3.34 ± 0.01	Ionization (erg cm s^{-1})
A_{Fe}	$4.4^{+0.4}_{-0.5}$	3.5 ± 0.2	Iron abundance (solar)
R	> 9.3	> 9.8	Reflection fraction
χ^2/dof	314/285	288/283	Fit statistic

Best-fit parameters excluding the absorption feature (model 1) and including it (model 2). Errors are 1σ . Parameters marked with asterisks are fixed at the stated value.

Extended Data Table 2 | Physical model fit

	Fe xxv	Fe xxvi
v (c)	0.244 ± 0.09	0.210 ± 0.009
$\log \xi$ (erg cm s ⁻¹)	4.0 ± 0.1	> 4.5
N_{H} 10 ²² cm ⁻²	8.2 ± 2.5	180 ± 50
σ_{v1D} (km s ⁻¹)	1500 ± 1000	1500 ± 1000

Best-fit physical model parameters for the stacked EPIC-pn spectrum. Errors are 1 σ .